

Implications of Promiscuous Pim-1 Kinase Fragment Inhibitor Hydrophobic Interactions for Fragment-Based Drug Design[†]

Andrew C. Good,^{*,‡} Jinyu Liu,[§] Bradford Hirth,[‡] Gary Asmussen,[§] Yibin Xiang,[‡] Hans-Peter Biemann,[§] Kimberly A. Bishop,[#] Trisha Fremgen,[§] Maria Fitzgerald,^{||} Tatiana Gladysheva,[§] Annuradha Jain,[#] Katherine Jancsics,[‡] Markus Metz,[‡] Andrew Papoulis,[‡] Renato Skerlj,[‡] J. David Stepp,[§] and Ronnie R. Wei[‡]

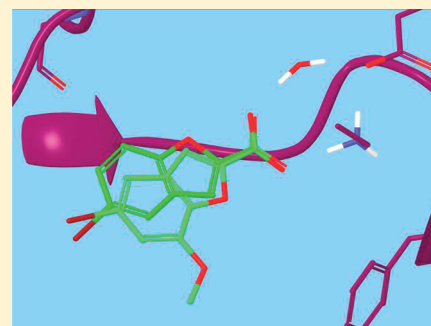
[‡]Department of Medicinal Chemistry, [§]Department of In Vitro Biology, and ^{||}Department of DMPK, Drug and Biomaterial R&D, Genzyme Corp., 153 Second Avenue, Waltham, Massachusetts 02451, United States

[‡]Department of Therapeutic Protein Research, Genzyme Corp., 1 Mountain Road, Framingham, Massachusetts 01701, United States

[#]Department of Therapeutic Protein Discovery, Genzyme Corp., 49 New York Ave., Framingham, Massachusetts 01701, United States

S Supporting Information

ABSTRACT: We have studied the subtleties of fragment docking and binding using data generated in a Pim-1 kinase inhibitor program. Crystallographic and docking data analyses have been undertaken using inhibitor complexes derived from an in-house surface plasmon resonance (SPR) fragment screen, a virtual needle screen, and a de novo designed fragment inhibitor hybrid. These investigations highlight that fragments that do not fill their binding pocket can exhibit promiscuous hydrophobic interactions due to the lack of steric constraints imposed on them by the boundaries of said pocket. As a result, docking modes that disagree with an observed crystal structure but maintain key crystallographically observed hydrogen bonds still have potential value in ligand design and optimization. This observation runs counter to the lore in fragment-based drug design that all fragment elaboration must be based on the parent crystal structure alone.



INTRODUCTION

The accepted wisdom around fragment-based drug design (FBDD) is that the challenges inherent to docking fragments render crystal structure data critical for ligand design. It is also generally accepted that fragments are harder to dock relative to larger drug sized molecules. More recent studies focusing on this issue, however, suggest that there is little difference in docking performance between the two.^{1,2} These investigations also surmise that incorrect docking of fragments tends to occur due to incorrect scoring, while for druglike molecules sampling issues are the primary problem. The scoring issue appears to be due to the fact that small energy differences often exist between fragment binding modes.¹ These differences are beyond the ranking resolution of existing scoring functions to differentiate, even when sampling is sufficient to find binding modes close to the observed crystal structure.

We have investigated these issues in the context of a legacy FBDD program run within Genzyme. The Pim family of serine/threonine kinases has been implicated as having a functional role in cell survival.³ This has provided a general mechanism for the potential of Pim kinases as targets in oncology and immunology regulation.^{4–6} Pim kinases are transcriptionally activated by FLT3,⁷ rendering them constitutively active.⁸ In addition, Pim kinase structures benefit from the presence of an unusual proline in the hinge region of

ATP binding site, which both expands the ATP pocket and alters the kinase hinge hydrogen-bonding motif.⁹ As a result of these features, the potential for finding selective small-molecule inhibitors for the Pim family relative to other kinases is significantly enhanced. On the basis of these and other data, Pim-1 was selected as a Genzyme oncology target and a drug discovery program initiated. Our primary strategy involved the application of fragment-based screening using surface plasmon resonance (SPR) to find early hit molecules, followed by X-ray structure guided medicinal chemistry optimization. The screen yielded a number of useful hits, one of which was rapidly optimized to high potency.¹⁰ A key facet of our drug discovery approach has been to continue focusing some resource on broadening our chemotype SAR even when entering hit/lead optimization. With that in mind, an analysis of the Genzyme screening deck was undertaken to find additional fragment-like inhibitors. The high concentration screening of such “needle” compounds in biochemical assays was pioneered at Roche,¹¹ and the technique has since been adapted to allow for high concentration screening of low complexity molecule collections in parallel with high throughput screening (HTS).¹² For this work, we returned to the original approach favored by Boehm

Received: October 31, 2011

Published: February 16, 2012

et al.¹¹ in which a 3D-constrained target-biased subset of compounds was chosen for screening from the available needles. Pim-1 was considered appropriate for this approach given the number of SPR fragment hits we found with potencies sensitive to a standard biochemical screen ($IC_{50} < 125 \mu\text{M}$).¹⁰

In concert with these hit-finding efforts, we leveraged our understanding of the key components of Pim-1 binding to explore potential new lead chemotype opportunities. These studies focused on an interesting Pim-1 screening hit for which a postulated binding mode had been published in what we deemed to be an incorrect orientation.¹³ The molecule was redocked and a chimera designed leveraging another Pim-1 inhibitor series postulated to share a similar binding mode.¹⁴ The results of these studies are described below, with a focus on the docking and crystal structure data gathered and their implications for FBDD.

RESULTS

Needle Screening. The Genzyme screening deck was analyzed using a simplified version of the Astex rule of 3 (molecular weight < 300 , $\text{ClogP} \leq 3$, and number of rotatable bonds ≤ 3).¹⁵ A total of 13 888 molecules passed this filter and became part of a virtual needle screening deck for the Glide docking program.¹⁶ At the time this screen was run, no in-house crystal structures of Pim-1 were available, so virtual screens were constructed using structures available in the Protein Data Bank (PDB).¹⁷ An analysis of available PDB structures highlighted the importance and diversity of hydrogen-bonding interactions in the vicinity of the catalytic domain lysine (K67). The variability comes about due to conformational switching of the c helix E89 residue producing a variety of gatekeeper water molecule hydrogen-bonding motifs. Searches were constructed based on the motifs observed in four Pim-1 inhibitor complexes^{18,19} (Figure 1), taking advantage of Glide's versatile pharmacophore constraint tools. Hydrogen-bond constraints were focused in the region of K67, with an additional positional constraint allowing aromatic carbons (all inhibitors shown in Figure 1 exhibit such interactions at this position) or hydrogen-bond donors in the vicinity of the E121 hinge carbonyl group (see Experimental Section for further details). The final selection of 500 compounds was checked for availability, resulting in 462 molecules chosen for screening. The IC_{50} s of all molecules showing $>50\%$ inhibition at $125 \mu\text{M}$ were determined, with 46 exhibiting IC_{50} s below $100 \mu\text{M}$ (the full structure list is shown in Supporting Information).

Six molecules were repurchased and recrystallized with the target both to confirm binding and determine binding mode. Comparisons between the crystallized and Glide docked structures of five of these molecules are shown in Figure 2 (the sixth molecule was an analogue of **2c** and was found to exhibit the same binding mode. It was thus excluded as it provides little additional insight).

Novel Lead Design. A survey of the literature highlighted **3** (Figure 3), a Pim-1 thiazolidinedione (THZ) screening hit with impressive potency and ligand efficiency (LE).¹³ The accompanying docking study suggested that the THZ hit formed a hydrogen bond between the amide hydrogen and the hinge carbonyl group of E121, while simultaneously interacting with the hydrophobic pocket under the P loop (F49). The primary issue with this docking calculation is that the THZ is protonated, while THZs are known to function as carboxylate

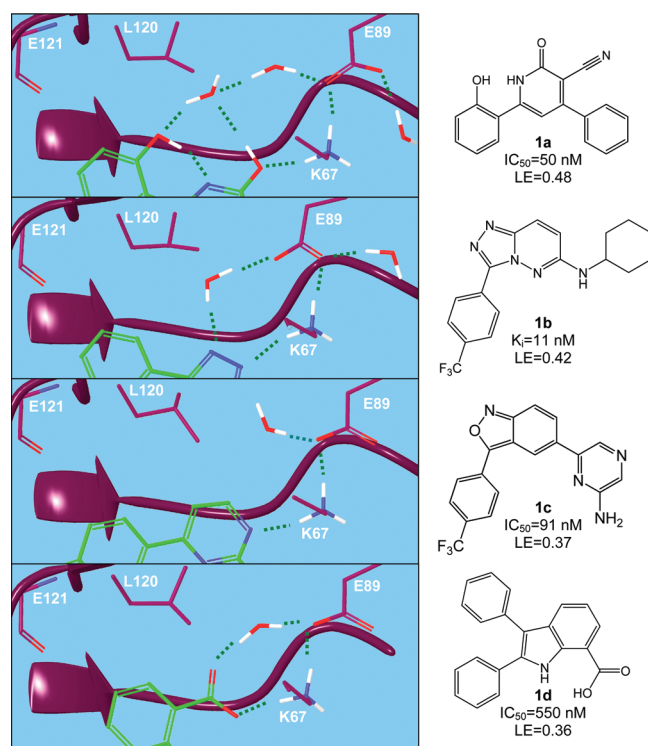


Figure 1. Hydrogen-bonding networks (green dotted lines for heteroatom distance $< 3.0 \text{ \AA}$) around catalytic domain K67 highlighted for each of the four structures used in virtual screening calculations. The 2D structures of the parent inhibitors associated with each complex are shown for reference, together with their Pim-1 IC_{50} / K_i data and LEs. The structures used are (a) **2OBJ**,¹⁸ (b) **3BGQ**,¹⁹ (c) **3BGP**,¹⁹ and (d) **3BGZ**.¹⁹ The conformational switching of E89 in structure b and the general variability in positioning and number of water-mediated hydrogen bonds are of particular note. For **1a** the hydroxypyridine tautomer was hypothesized as preferred due to the presence of a stabilizing internal H bond from the pendant phenolic hydroxyl. It was this tautomer that was used in protein preparation. If the generally preferred pyridone tautomer is used instead, the pendant phenolic hydroxyl hydrogen can no longer form either an inter- or intramolecular hydrogen bond, as it cannot pair with the gatekeeper water. This leads to an unpaired hydrogen bond donor exposed to a hydrophobic environment. We suspect that the internal hydrogen bond and the ortho cyano substituent stabilize this tautomer or allow the formation of the phenolate anion given the preference of this active site region to bind acidic functionality.

mimics in PPAR γ agonists.²⁰ We had already found a number of carboxylate-containing fragment hits in our original SPR fragment screen¹⁰ (molecules **4a** and **4b**, Figure 4), and this led us to believe that the THZ was most likely deprotonated on binding. With this in mind, **3** was redocked using Glide [standard precision (SP) and extra precision (XP)] into the crystal structure of **4a** (PDB code 3R00), the most ligand efficient acid discovered in the SPR screen. The Glide SP results were studied in depth as they both reproduced the expected hydrogen-bonding interactions and returned multiple binding modes for visual inspection. The top scoring docking modes are shown in Figure 5. An alternate docking (the fifth docking mode in the Glide SP calculation) is shown in Figure 6. At this point a new Pim-1 structure was deposited in the PDB based on a novel series of carboxylate inhibitors determined in an HTS screen (compound **5**, PDB code 3F2A; see Figure 7).¹⁴ Superposition of the alternate docking mode of **3** with the crystal structure of **5** suggested the possibility of creating a

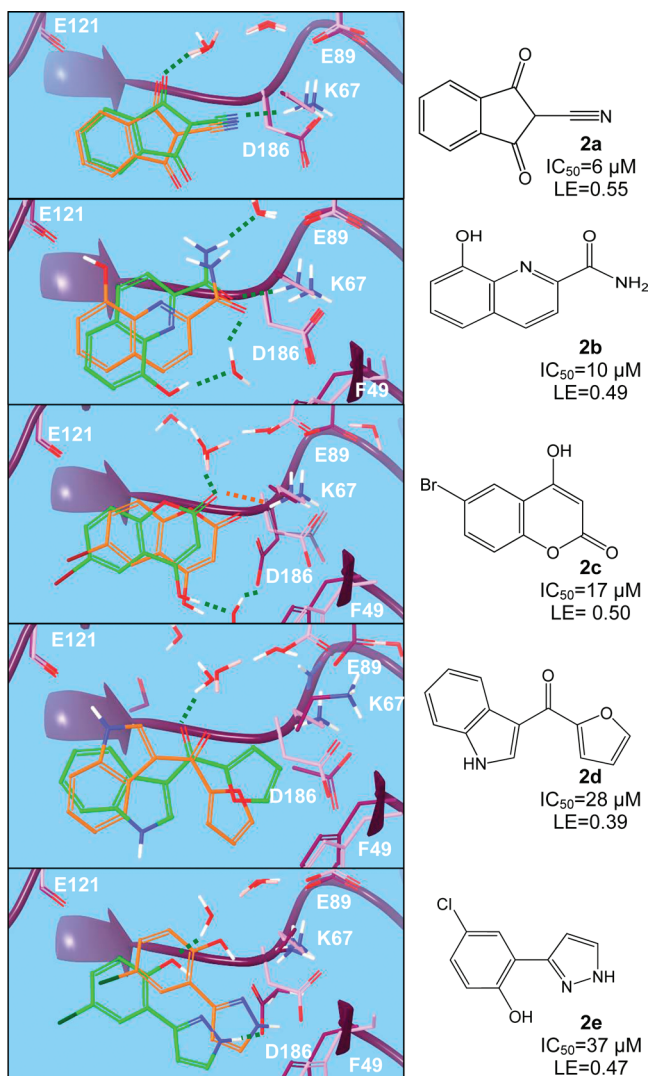


Figure 2. Top scoring docked structures (orange ligand and pink protein) and crystal structure (green ligand and purple protein) for five hits from the needle screen. The reference structure is taken from the top score generating reference structure in each case. Note that water molecules associated with each reference structure are shown with pink hydrogens. 2D structures, Pim-1 IC_{50} s, and LEs are shown for each ligand and key hydrogen bonds are highlighted (green dotted lines for heteroatom distance $< 3.0 \text{ \AA}$, orange for distance $\sim 3.2 \text{ \AA}$). The PDB codes of the crystal structure of these compounds are as follows: (a) 3VBW, (b) 2VBV, (c) 3VBX, (d) 3VBY, and (e) 3VBT. Note that **2a** may exist as an enolate tautomer; however, this is not how it was modeled in the virtual screening studies. Note also that for **2c** an alternate location is included for D186.

chimera molecule linking through the trifluoromethyl bond (Figure 7). Chimera design based on this superposition using

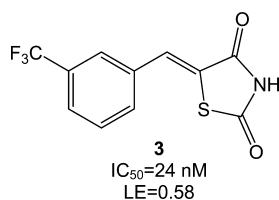


Figure 3. Pim-1 THZ screening hit¹³ used in chimera lead design with Pim-1 IC_{50} and LE shown for reference.

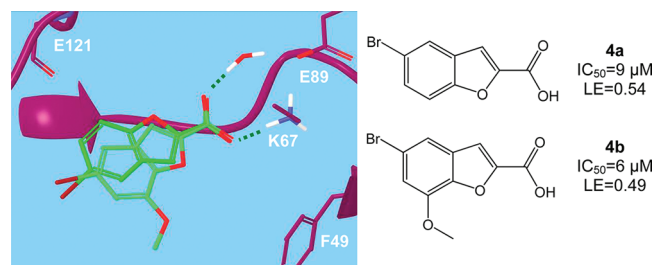


Figure 4. Crystal structures of carboxylate-containing hits from internal SPR fragment screen¹⁰ [PDB reference codes 3R00 (**4a**) and 3R01 (**4b**)]. Key hydrogen bonds are highlighted with Pim-1 IC_{50} s and LEs shown for reference. Note that the protein structures of these complexes have essentially identical tertiary structure.

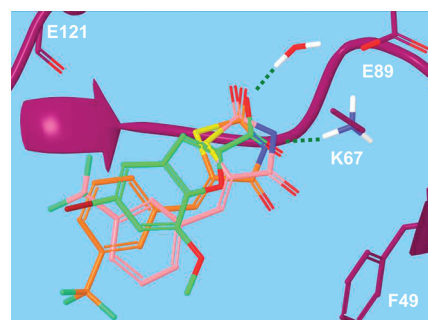


Figure 5. THZ crystal structure of **3** (pink) versus unconstrained Glide XP/SP highest scoring docking modes (identical and in orange), with **4b** crystal structure (green) of carboxylate-containing hit shown for reference. Proteins of both crystal structures are also essentially superimposable, so only the protein structure of **4b** has been included. The crystal structure of **3** has been deposited in the PDB using code 3VC4.

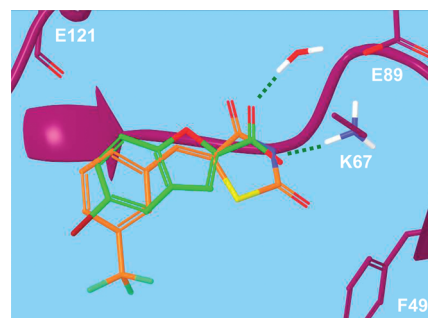


Figure 6. Alternate Glide SP docking mode for deprotonated model of **3** (orange) superimposed on reference crystal structure **4a** (green) used in docking.

the most potent fragment abstracted from the original reference¹⁴ produced **6** (Figure 8). The top scoring Glide docking modes for **6** agreed with the postulated binding mode (Figure 8). Synthesis of **6** produced an inhibitor of Pim-1 with an IC_{50} of 467 pM. The crystal structure of **6** is shown in Figure 8. Note that the crystal structure binding mode of **3** is also shown in Figure 5. This was solved subsequent to the design and synthesis of **6**.

DISCUSSION

The crystal structures for the needle screen hits shown in Figure 2 highlight all the classic pitfalls that can trip up docking calculations. Protein residues and water molecule positions in

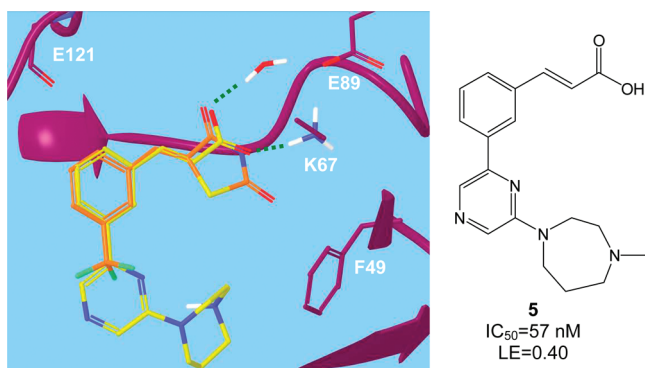


Figure 7. Alternate Glide SP docking mode of **3** (orange) superimposed on crystal structure of molecule **5** (PDB code 3F2A). The protein reference structure shown is also derived from 3F2A. Pim-1 IC_{50} and LE of **5** shown for reference.

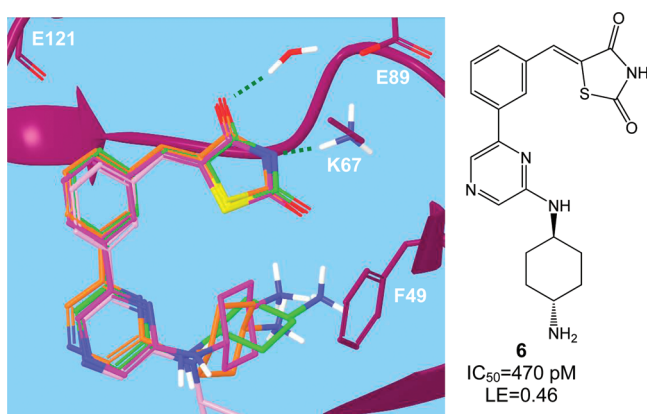


Figure 8. Crystal structure of **6** (green) superimposed on constrained Glide SP (orange), unconstrained Glide SP (pink), and Glide XP (maroon) top scoring binding modes on docking to the crystal structure of **5** (key hydrogen bonds highlighted). The crystal structure of **6** has been deposited in the PDB using code 3VBQ.

the structure around **2a** match those of the structure used for docking (from protein complex of molecule **1a**) closely, and the resulting docking mode is a close match to the crystal structure (rmsd 0.88 Å). The gatekeeper water interaction between the crystal structure of **2b** and its docking reference structure (**1c**) is also well-matched, resulting in a good superposition of amide hydrogen-bonding interactions between docked and crystallographic binding modes. The inability of docking calculations to deal with shifting water molecule positions confounds the positioning of the hydroxyquinoline ring, however. The docking model postulates an internal hydrogen bond with the hinge carbonyl group of E121, while in reality the phenolic hydroxyl forms an internal water-mediated hydrogen bond and flips to interact with F49 on the P loop. This is perhaps not surprising, as the preference for aromatic CH interactions with the hinge carbonyl group has precedence²¹ and is well-documented in existing Pim-1 inhibitors (Figure 1). As a consequence, while the key hydrogen-bonding motif constraint is correctly matched, the rmsd is still 2.6 Å between docked and crystallographic binding modes. To test the effects of the constraints on the search, an unconstrained Glide SP calculation was also run on **2b** in the **1c** active site. This search yields the same top scoring docking mode as seen in Figure 2, showing that the presence of the docked mode hinge interaction is not due solely to the positional constraint used.

The closest rmsd (which is the second top scorer) found in the constrained searches is 1.1 Å (Figure 9, pink structure), with

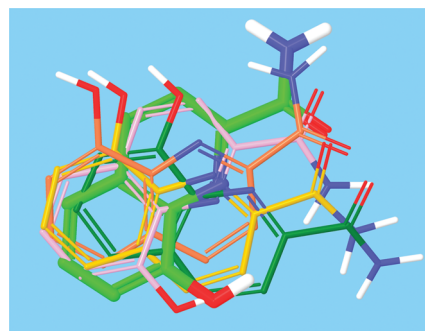


Figure 9. Crystal structure (light green) and the docked binding modes of **2b** for the four virtual screens run. Ligands have been extracted from their respective binding poses after superposition of the Pim-1 references structures used in docking.

the quinoline rings nearly superimposed but with the hydrogen-bonding interactions completely disrupted. The highest scoring docking mode for **2c** (**1b** used for docking) is found to superimpose well with the crystal with an rmsd of 1.0 Å. This is a case where a good docking mode is obtained despite the changes occurring around the ligand on binding. E89 shifts position to accommodate no less than 3 water molecules in the gatekeeper pocket, fortunately without disrupting the position of the key water-mediated hydrogen bond. In addition, D186 lifts up in the site to form a water-mediated hydrogen bond with the hydroxyl off the back of the coumarin ring, again with little effect on the binding mode. A slight shift in hydrogen-bonding interactions is seen, with the docking mode seemingly overemphasizing the potential for hydrogen bonding with the ester oxygen of the coumarin ring. Instead, the molecule shifts to permit a bifurcated interaction between K67 and the gatekeeper water molecule. Molecule **2d** produces shifts in the active site that begin to confound the docking calculation (to **1b**) to a significant degree. In particular, the side chain of K67 lifts up in the active site to allow the furan ring to sit in a hydrophobic sandwich between the carbon side chain atoms of K67 and D186. This interaction is impossible to replicate in any of the sites used for docking and a high rmsd ensues (2.9 Å). Nevertheless, the key water-mediated hydrogen bond to the carbonyl oxygen is essentially maintained, but as in the case of **2b**, the formation of a hydrogen bond to the hinge (this time through the indole nitrogen) proves irresistible. For molecule **2e**, we see a complete breakdown in docking mode accuracy both from an rmsd (2.3 Å) and interaction standpoint. The reference docking structure that produces the highest Glide score (**1d**) shows no conservation in water-mediated hydrogen-bonding interactions and does not take into account the shift in position of D186, which also forms a key hydrogen bond with pyrazole of **2e**.

If we look at the overall performance of the docking calculations, while only two of the highest scoring docked modes are docked correctly in their entirety, four of five systems correctly map the key hydrogen-bonding constraints. This once again highlights the utility of incorporating hydrogen-bonding constraints, even when screening for fragment-sized hits. It also underlines the value of crystal structures given the resolution limits of docking scores,

particularly in the context of changes in water molecule binding patterns and side chain shifts.

To explore the notion of flat energy surfaces from a more quantitative perspective, the difference in scores between top scoring docked and crystal structure binding modes has also been explored. The use of postscore minimization in enhancing docking accuracy was recently shown to have potential in fragment docking.¹ With this in mind and to allow for relaxation of the crystal structure on cross-docking, all docked, cross-docked crystal and native crystal structures were refined using Impref-constrained minimizations (see Experimental Section). The resulting binding modes were then rescored using Glide SP. The degree of diversity in the docked poses produced for each hit has been explored by studying both the count of duplicate binding modes and hinge hydrogen-bonding propensity. The results of these studies are shown in Table 1

Table 1. Additional Docking Data for Hits 2a–e^a

compound	top docked complex	transplanted X-ray ligand	native X-ray structure	consensus/duplicate/hinge H bond count
2a	−7.4	−7.9	−7.8	4/2/0
2b	−9.0	−7.7	−8.0 /−9.3 ^b	4/0/2
2c	−7.1	−7.0	−7.0	2/2/0
2d	−9.1	1000 ^c	−8.4	3/0/2
2e	−7.8	−5.7	−7.7	3/0/0

^aColumns 2–4 summarize the Glide SP scores of Impref-refined needle screen hit complexes for the top docked ligand, the X-ray ligand binding mode in the top scoring docking complex protein, and the native X-ray structure. Column 4 shows the number of times inhibitor met the −6 score cutoff for the four searches run/the number of duplicate binding modes (RMSD < 0.5 Å) observed/number of times that a hydrogen bond to hinge was observed. ^bScores with and without the presence of water molecule bridging phenol and carbonyl groups. ^cCalculation contains a significant clash with docking protein.

and Figure 9. Molecules 2a and 2e both show little difference in scoring between the cross-docked crystal, native crystal, and virtual screening docked structures. One might expect this given the high level of similarity of the native and docked binding modes. It is nonetheless interesting that, although Glide's hbond score has increased from −0.29 to −0.49 in the presence of an interstitial water molecule in the native 2c structure, there is little overall effect in the Glide SP score. It is also of note that these are the two inhibitors with highest LE, given that the correlation between said efficiency and docking accuracy has been observed previously.¹ For 2b, the virtual screening score is higher than the cross-docked X-ray crystal structure score by a significant margin. The refined native crystal structure scores the highest, but only when the interstitial water molecule that sits between the carbonyl and phenol groups is retained. If this is removed, the resulting score is similar to the docked mode. This highlights both potential effects of interstitial water (in contrast to 2c), which increases the Glide hbond score from −0.48 to −1.01 while also increasing both Glide reward and Glide Emodel contributions. Molecule 2d has no cross-docking scores, as the clash between the crystal structure inhibitor and the docking protein prevents a successful docking mode from being formed. For 2e, while the cross-docked crystal inhibitor can be scored, the lack of interactions with D186 in the docking protein relative to the native structure compromises the score, highlighting the potential importance of side chain conformation changes. For

2d, the top-scoring docked complex out scores the native binding mode, with a significant part of the difference derived from the hinge hydrogen bond contribution (Glide hbond score −0.61 vs −0.32, respectively). For 2e, although the docked and native binding modes are quite distinct, the resulting Glide SP scores are similar, an example of scoring resolution issues when docking fragments. For 2b and 2d, the two systems for which there are hinge hydrogen bonds observed in the virtual screens, two of four modes for 2b and two of three modes for 2d show this interaction. Overall, however, there is little duplication in binding modes between the top scoring hits from each virtual screen, with the high diversity of hydrogen-bonding constraints around K67 creating a wide array of binding configurations (Figure 9).

The results above suggest that while docking is useful for finding hits, crystal structure data are indeed critical for FBDD molecular design. This presupposes, however, that the binding energy differences between crystal and docked modes are generally large enough to render the docking mode useless. A closer look at the binding mode changes seen in the carboxylate- and THZ-containing chemotypes show that this is not always the case. The potential for binding mode shifts inherent in hydrophobic interactions with few shape constraints is nicely illustrated by the benzofuran carboxylate containing analogue SPR hits shown in Figure 4. While the addition of a methoxy produces a steric-clash-induced ring flip, the lack of additional shape constrained interactions allows this to occur while both key hydrogen bonds and binding potency are maintained. This is a potential feature of fragment binding, since they often do not completely fill an active site, with the result that their shapes are unable to act as a strong directional constraint. This, as well as the importance of understanding key hydrogen-bonding interactions in an active site, is nicely illustrated in the chimera inhibitor design example of 6. An understanding of the hydrogen-bonding preferences of Pim-1 led to the correct assertion of the THZ binding of 3 occurring via K67 and water-mediated hydrogen bonds through a deprotonated headgroup. The top scoring Glide SP docking mode (score −8.4) showed the hydrophobic portion of 3 binding in a 4b-like manner (Figure 5). An alternate docking mode of 3 (Figure 6, score −6.8) places its phenyl group deeper into the pocket (similar to 4a and 5). Given the conformational flips already observed in the carboxylate-containing inhibitors and the excellent mapping of this docking mode onto 5 (Figure 7), we decided to pursue the synthesis of 6. This proved a wise choice, as the activity of 6 is over 20 times greater than the most potent compounds from either parent series, with a LE higher than the original lead 5. The crystal structure of 6 (Figure 8), which is in agreement with the Glide docking calculation, confirms the binding hypothesis. Interestingly, the crystal structure of 3 (Figure 6, solved subsequent to initiation of molecule 6 synthesis) confirms THZ binding in acidic form but shows a flipped orientation for the hydrophobic portion of the molecule, closer to the top scoring Glide SP docking mode. Glide SP data for 3 highlights a preference for binding the trifluoromethyl along rather than toward the hinge. This is illustrated by the fact that two of the ten Glide SP docking modes are within 1 Å rmsd of the crystal structure but score significantly lower (−6.8 and −6.8 versus −8.4). These results are consistent with the observations of Verdonk et al., which point to scoring rather than sampling as the biggest obstacle to accurate fragment docking.¹ As a consequence, molecular design based on docking derived binding modes

remains a technique worthy of consideration when used appropriately.

CONCLUSIONS

We have used data extracted from our Pim-1 project efforts to further investigate the subtleties of fragment inhibitor binding. The success of our needle screen at retrieving actives and the ability of the constrained docking calculations used to reproduce the crystallographically observed primary hydrogen-bonding patterns are noteworthy. It is nevertheless clear that, as one might expect, crystal complexes are still key to understanding the subtleties of fragment binding, particularly in regard to new water molecule interactions and side chain shifts. When water and side chain sampling are not an issue, our data point toward fragment scoring rather than binding mode sampling as the primary docking limitation, in keeping with earlier studies. Our subsequent chimera inhibitor design study suggests, however, that fragment docking modes for which hydrophobic interactions are in disagreement with the parent crystal structure may still have value when key hydrogen bonds are maintained. While the design was based on a docking mode for which the hydrophobic interactions were found to be incorrect by crystallography, the predicted binding mode of the resultant highly potent chimera was nonetheless confirmed. The data presented here highlight the low level of hydrophobic interaction directionality possible when fragment hits do not completely fill the pocket to which they bind. This lack of directionality can both confound docking scores and provide additional design opportunities based on alternate “incorrect” docking poses during fragment elaboration.

EXPERIMENTAL SECTION

Modeling. All virtual screening and docking experiments were carried out within the Maestro suite of software.²² All protein complexes were prepared using the protein preparation wizard workflow by applying default settings (preprocess keeping water molecules within 5 Å of ligand, water optimization sampling with interactive optimization of gatekeeper water molecule hydrogen positions where appropriate, followed by Impref refinement to 0.3 Å rmsd). Glide¹⁶ was used to perform all docking experiments by applying the default calculation settings. The reference proteins used in each calculation are detailed in the Discussion and Results sections. Glide SP was used for all virtual screening experiments, while both Glide XP and Glide SP were applied to individual compound docking studies. For each virtual screen hydrogen-bonding constraints were placed on K67 and any relevant gatekeeper water molecules shown to create water-mediated hydrogen bonding with the complexed inhibitor. In addition, a 1.0 Å radius positional constraint was added on the basis of the position of the nearest inhibitor aromatic carbon atom of each complex to the inner hinge backbone carbonyl group of E121, with aromatic carbon atoms and heteroatom hydrogen bond donors being allowed to map the constraint. For each search, the positional constraint and a hydrogen bond match up to either the gatekeeper water molecule and/or K67 were required for a total of eight searches. Comparison of the “and” versus “or” hydrogen bond constraint searches showed significant overlap of results of compound binding modes and selections, so the “and” searches were dropped from the analysis. The top scoring hit for each molecule was retained for each virtual screen run, and this resulted in a total of 1927 hits scoring –6 or less using Glide SP.¹⁶ This score was used to define a threshold for general relevance, which from our perspective was the limit of its resolution given all the uncertainties inherent in docking. The hit lists were combined and reordered multiple times using a number of the scoring columns provided by the Glide calculation (docking score, glide lipo, glide h bond, and glide ligand efficiency). In each case, the hit lists were then analyzed visually within Vida, which is

well-suited for rapid visual analysis of large data sets.²³ Compounds were selected primarily on the basis of the observed diversity of hydrogen bond interaction(s) in the vicinity of K67, together with an experienced eye “this looks reasonable and interesting” criteria. Multiple analogues were chosen for particularly interesting chemotypes to hedge against potential purity issues, given that the compounds were taken from DMSO stock rather than direct from solid as is the case for fragment deck screens. Selections were also focused on compounds appearing in the hit list multiple times (i.e., with a Glide score < –6 in multiple searches), providing a qualitative consensus scoring bias. All database molecules were prepared using Ligprep²⁴ with tautomer probability set to 30, maximum tautomers equal to 4, maximum stereoisomers set to 2, with a maximum of two ring conformations being equal using idealized geometries and both neutral and charged molecule generation permitted.

For the inhibitor docked and crystal structure binding mode comparisons in Table 1, the crystal structure protein and the parent virtual screening protein for the top scoring docking mode of each hit (2a–e) were superimposed. The crystal structure of each inhibitor was then abstracted into the virtual screening protein to create a cross-docking mode of each hit crystal structure. This then underwent a constrained minimization using the Impref routine in the protein preparation wizard of Maestro 9.2.0.15²² (maximum heavy atom rmsd shift permitted during minimization set to 0.3 Å using the OPLS 2005 force field). The same Impref routine was also used to minimize each top scoring docked pose to provide a consistent frame of reference. In the same vein each crystal structure also underwent a full protein preparation (including an Impref refinement). All the resulting refined conformations were then rescored using Glide SP (version 57109).

For the chimera design, 3 was docked with the THZ deprotonated. For this study the top 10 scoring ligand binding poses were retained from the Glide SP docking experiment with each analyzed visually.

Chemistry. All solvents and reagents were used as purchased from various commercial sources. Reactions were conducted under a dry nitrogen atmosphere unless otherwise indicated. Chromatography was carried out using a Teledyne Isco Combiflash R_f system employing prepacked RediSep silica cartridges. ¹H and ¹³C NMR spectra were acquired on a Bruker Ultrashield 400 instrument operated at 400 and 100 MHz, respectively. NMR samples were prepared as CDCl₃ or DMSO-*d*₆ solutions and referenced as follows: ¹H NMR, TMS (δ = 0.00 ppm); ¹³C NMR, DMSO-*d*₆ (δ = 39.52 ppm). The purity of 6 was determined using a Waters Acquity UPLC system equipped with an Acquity PDA detector and in-line Waters ZQ2000 mass spectrometer (ESI). UPLC conditions were as follows: column, Acquity UPLC BEH C18 (2.1 × 50 mm, 1.7 μ m); column temperature, 50 °C; flow rate, 1.0 mL/min; mobile phase A, 0.1% formic acid in water; mobile phase B, 0.1% formic acid in acetonitrile; gradient, 5%–95% B (0–1.9 min), 95% B (1.9–2.2 min), 95%–5% B (2.2–2.3 min), 5%–0% B (2.3–10 min). Purity was calculated as a percentage of total area at 210 and 254 nm.

(Z)-5-(3-(6-((trans-4-Aminocyclohexyl)amino)pyrazin-2-yl)-benzylidene)thiazolidine-2,4-dione 2,2,2-Trifluoroacetate (Compound 6). *Step 1.* To a stirred solution of *trans*-1,4-diaminocyclohexane (3.90 g, 34.1 mmol) and 2,6-dichloropyrazine (2.04 g, 13.7 mmol) in 1,4-dioxane (100 mL) was added diisopropylamine (5.9 mL, 34 mmol). The mixture was heated at reflux for 16 h and then concentrated. The residue was taken up in aqueous sodium bicarbonate solution (~150 mL) and extracted with dichloromethane (3 × ~100 mL). The combined extracts were dried over sodium sulfate and concentrated. The resulting oil was purified by flash chromatography over silica (5–15% gradient of 2 N ammonia/methanol in methylene chloride) to provide *trans*-N-(6-chloropyrazin-2-yl)cyclohexane-1,4-diamine as tacky tan solid (2.12 g, 69%): ¹H NMR (CDCl₃) δ 7.75 (s, 1H), 7.70 (s, 1H), 4.66 (d, *J* = 7.4 Hz, 1H), 3.78–3.56 (m, 1H), 3.47 (s, 3H), 2.81–2.63 (m, 1H), 2.18–2.04 (m, 2H), 2.03–1.83 (m, 2H), 1.63 (s, 5H), 1.38–1.14 (m, 4H) ppm.

Step 2. To a stirred solution of step 1 product (2.12 g, 9.37 mmol) in methylene chloride (90 mL) was added di-*tert*-butyl dicarbonate

(2.45 g, 11.2 mmol). The solution was stirred at room temperature for 16 h and then washed with aqueous sodium bicarbonate (~75 mL), dried over sodium sulfate, and concentrated. The resulting solid was purified by flash chromatography over silica (0–5% gradient of methanol in methylene chloride) to provide *tert*-butyl (*trans*-4-((6-chloropyrazin-2-yl)amino)cyclohexyl)carbamate as a tan solid (2.30 g, 75%): ¹H NMR (CDCl₃) δ 7.76 (s, 1H), 7.70 (s, 1H), 4.55 (d, *J* = 7.9 Hz, 1H), 4.50–4.28 (m, 1H), 3.77–3.61 (m, 1H), 3.61–3.39 (m, 1H), 2.20–2.12 (m, 2H), 2.12–2.02 (m, 2H), 1.45 (s, 9H), 1.36–1.19 (m, 4H) ppm.

Step 3. Step 2 product (1.00 g, 3.07 mmol), 3-formylphenylboronic acid (0.506 g, 3.37 mmol), and potassium carbonate (2.97 g, 21.5 mmol) were taken up in DMF (35 mL) and water (10 mL). Nitrogen was bubbled through the stirred mixture for 15 min. Following degassing, bis(triphenylphosphine)palladium(II) dichloride (0.054 g, 0.077 mmol) was added and the mixture was heated at 100 °C for 1.5 h. The reaction was then concentrated and the residue partitioned between ethyl acetate (~70 mL) and water (~100 mL). The organic layer was washed with additional water (2 × ~100 mL), dried over sodium sulfate, and concentrated. The resulting tan solid was purified by flash chromatography over silica (0–5% gradient of methanol in methylene chloride). *tert*-Butyl (*trans*-4-((6-(3-formylphenyl)pyrazin-2-yl)amino)cyclohexyl)carbamate was afforded as a light yellow solid (1.12 g, 92%): ¹H NMR (400 MHz, CDCl₃) δ 10.11 (s, 1H), 8.49–8.46 (m, 1H), 8.32 (s, 1H), 8.25–8.21 (m, 1H), 7.96–7.91 (m, 1H), 7.84 (s, 1H), 7.67–7.61 (m, 1H), 4.62 (d, *J* = 7.6 Hz, 1H), 4.54–4.38 (m, 1H), 3.88–3.74 (m, 1H), 3.59–3.41 (m, 1H), 2.29–2.05 (m, 4H), 1.46 (s, 9H), 1.44–1.28 (m, 4H) ppm.

Step 4. To a stirred suspension of step 3 product (1.10 g, 2.77 mmol) and 2,4-thiazolidinedione (0.341 g, 2.91 mmol) in *tert*-butanol (20 mL) was added piperidine (0.22 mL, 2.22 mmol). The mixture was heated at reflux overnight, cooled slightly, and suction filtered to remove suspended solid. The filter cake was rinsed with ethanol (2 × ~5 mL) and diethyl ether (2 × ~15 mL). Drying on the filter frit under house vacuum provided *tert*-butyl (*trans*-4-((6-(3-((*Z*)-(2,4-dioxothiazolidin-5-ylidene)methyl)phenyl)pyrazin-2-yl)amino)cyclohexyl)carbamate as a pale yellow solid (0.862 g, 63%): ¹H NMR (400 MHz, DMSO-*d*₆) δ 12.67 (br s, 1H), 8.35–8.31 (m, 1H), 8.29 (s, 1H), 8.13–8.08 (m, 1H), 7.89 (s, 1H), 7.87 (s, 1H), 7.72–7.67 (m, 1H), 7.65–7.60 (m, 1H), 7.14 (d, *J* = 7.3 Hz, 1H), 6.52 (d, *J* = 8.0 Hz, 1H), 4.26–4.07 (m, 1H), 3.90–3.72 (m, 1H), 2.15–1.98 (m, 2H), 1.95–1.77 (m, 2H), 1.39 (s, 9H), 1.39–1.23 (m, 4H) ppm.

Step 5. To a stirred suspension of step 4 product (0.300 g, 0.605 mmol) in methylene chloride (8 mL) was added trifluoroacetic acid (2.0 mL, 26 mmol). After 45 min the reaction was concentrated. The residue was further dried in a vacuum oven (60 °C) overnight. The title compound was afforded as a bright yellow solid (0.317 g, 100%): ¹H NMR (400 MHz, DMSO-*d*₆) δ 12.70 (br s, 1H), 8.32–8.20 (m, 2H), 8.12–8.03 (m, 1H), 7.98–7.77 (m, 5H), 7.71–7.53 (m, 2H), 7.20 (br s, 1H), 3.87–3.66 (m, 1H), 3.15–2.95 (m, 1H), 2.24–1.88 (m, 4H), 1.58–1.22 (m, 4H) ppm; ¹³C NMR (100 MHz, DMSO-*d*₆) δ 167.7, 167.3, 158.3 (d, *J* = 34.3 Hz; TFA), 153.6, 146.9, 137.9, 133.5, 132.8, 131.5, 131.1, 129.7, 127.4, 127.2, 124.0, 116.3 (q, *J* = 29.4 Hz; TFA); UPLC purity 100% (210 nm), 98% (254 nm); retention time, 0.74 min; ESMS *m/z* 396.2 (M + H).

Pim-1 Dose–Response Assay. Reagents and consumables were purchased from Sigma Aldrich or Caliper Life Sciences. Human Pim-1 was produced internally at Genzyme. All assay reaction conditions for IC₅₀ determinations were within the linear range with respect to time and enzyme concentration. In a 384-well polypropylene plate, human Pim-1 (1.2 nM) was preincubated with a compound in a 100 mM Hepes–NaOH pH 7.5 buffer containing 0.01% Triton X-100, 10 mM MgCl₂, 0.1% BSA, 1 mM DTT, 10 μM sodium orthovanadate, 10 μM β-glycerophosphate, and 2.5% DMSO for 15 min at room temperature. The reaction was initiated with an equal volume of a peptide substrate (S-FAM-RSRHSSYPAGT-CONH₂, Caliper Life Sciences) and ATP mixture in the aforementioned buffer. The final concentrations in the reaction were 600 pM Pim-1, 1 μM peptide substrate, and 150 μM ATP (ATP Km). The reaction was incubated at room temperature for 45 min and terminated with a buffer containing

excess EDTA (100 mM Hepes–NaOH pH 7.5, 0.02% Brij, 0.1% CR-3, 0.36% DMSO, and 100 mM EDTA). The plate was run for one cycle on a LabChip 3000 (Caliper Life Sciences, Hopkinton, MA) in an off-chip mobility shift assay with an upstream voltage of –2250 V, a downstream voltage of –500 V, and a vacuum pressure of –1.6 psi. The LabChip 3000 separates and measures the fluorescent signal of fluorescein-labeled peptide substrate and fluorescein-labeled peptide product present in each well. Results are expressed as percent conversion by measuring peak heights for both the substrate and product and dividing the product peak height by the sum of peak heights for both substrate and product. On every plate 100% inhibition (with a saturating concentration of staurosporine) and 0% inhibition (substrate with enzyme and DMSO) controls were used to calculate percent inhibition of tested compounds and a *Z'*-value.²⁵

Crystallography. Purified human Pim-1 protein (aa 29–313) with a C-terminal His tag was concentrated to 10–13 mg/mL in 20 mM HEPES, pH 8, 120 mM NaCl, 5 mM DTT. Pim-1 was crystallized in 0.1 M imidazole, pH 6.4, anhydrous 1–1.4 M sodium acetate by sitting drop vapor diffusion at 4 °C and reached a maximum size after about 5 days. Pim-1 crystals were soaked with 10 mM compound in the well solution overnight at 4 °C and flash frozen with 30% glycerol in the presence of the compound. Diffraction data were collected at home and at ALS503 (Advanced Light Source at Lawrence Berkeley National Laboratory, Berkeley, CA) and processed using HKL2000 and Scala. Crystals belong to space group *P65*, with *a* = *b* = 98 Å, *c* = 80 Å, *α* = *β* = 90.00°, *γ* = 120.00°. The structures were solved by molecular replacement using the apo Pim-1 structure as a search model.²⁶ Iterative manual model building was carried out with Coot,²⁷ coupled with refinement using Refmac5. The resolutions (Å) of the structures elucidated were as follows: 2a, 2.48; 2b, 2.08; 2c, 2.03; 2d; 2.27; 2e, 2.23; 3, 2.23; 6, 1.85.

■ ASSOCIATED CONTENT

📄 Supporting Information

IC₅₀s and structures of all needle screening hits with a Pim-1 IC₅₀ < 100 μM. This material is available free of charge via the Internet at <http://pubs.acs.org>.

Accession Codes

†Crystal structure PDB IDs for inhibitors disclosed in this paper: 3VBQ, 3VBT, 3VBV, 3VBW, 3VBX, 3VBY, and 3VC4.

■ AUTHOR INFORMATION

Corresponding Author

*E-mail: andrew.good@genzyme.com. Tel: 781 464 3831. Fax: 781 290 5890.

Notes

The authors declare no competing financial interest.

■ ABBREVIATIONS USED

FBDD, fragment-based drug design; HTS, high-throughput screening; LE, ligand efficiency; PDB, Protein Data Bank; SAR, structure–activity relationship; SP, standard precision; SPR, surface plasmon resonance; THZ, thiazolidinedione; XP, extra precision

■ REFERENCES

- (1) Verdonk, M. L.; Giangreco, I.; Hall, R. J.; Korb, O.; Mortenson, P. N.; Murray, C. W. Docking performance of fragments and druglike compounds. *J. Med. Chem.* **2011**, *54*, 5422–5431.
- (2) Sándor, M.; Kiss, R.; Keserü, G. M. Virtual fragment docking by Glide: A validation study on 190 protein–fragment complexes. *J. Chem. Inf. Model.* **2010**, *50*, 1165–1172.
- (3) Amaravadi, R.; Thompson, C. B. The survival kinases Akt and Pim as potential pharmacological targets. *J. Clin. Invest.* **2005**, *115*, 2618–2624.

- (4) Amson, R.; Sigaux, F.; Przedborski, S.; Flandrin, G.; Givol, D.; Telerman, A. The human protooncogene product p33pim is expressed during fetal hematopoiesis and in diverse leukemias. *Proc. Natl. Acad. Sci. U. S. A.* **1989**, *86*, 8857–8861.
- (5) Shah, N.; Pang, B.; Yeoh, K-G; Thorn, S.; Chen, C. S.; Lilly, M. B.; Salto-Tellez, M Potential roles for the PIM-1 kinase in human cancer—A molecular and therapeutic appraisal. *Eur. J. Cancer* **2008**, *44*, 2144–2151.
- (6) Magnuson, N. S.; Wang, Z.; Ding, G.; Reeves, R. Why target PIM-1 for cancer diagnosis and treatment? *Future Oncol.* **2010**, *6*, 1461–1478.
- (7) Kim, K. T.; Levis, M.; Small, D. Constitutively activated FLT3 phosphorylates BAD partially through Pim-1. *Br. J. Haematol.* **2006**, *124*, 500–509.
- (8) Qian, K. C.; Wang, L.; Hickey, E. R.; Studts, J.; Barringer, K.; Peng, C.; Kronkaitis, A.; Li, J.; White, A.; Mische, S.; Farmer, B. Structural basis of constitutive activity and a unique nucleotide binding mode of human Pim-1 kinase. *J. Biol. Chem.* **2005**, *280*, 6130–6137.
- (9) Schenone, S.; Tintori, C.; Botta, M. Using insights into Pim-1 structure to design new anticancer drugs. *Curr. Pharm. Des.* **2010**, *16*, 3964–3978.
- (10) Xiang, Y.; Hirth, B.; Asmussen, G.; Biemann, H. P.; Bishop, K. A.; Good, A.; Fitzgerald, M.; Gladysheva, T.; Jain, A.; Jancsics, K.; Liu, J.; Metz, M.; Papoulis, A.; Skerlj, R.; Stepp, J. D.; Wei, R. R. The discovery of novel benzofuran-2-carboxylic acids as potent Pim-1 inhibitors. *Bioorg. Med. Chem. Lett.* **2011**, *21*, 3050–3056.
- (11) Boehm, H.-J.; Boehringer, M.; Bur, D.; Gmuender, H.; Walter, H.; Klaus, W.; Kostrewa, D.; Kuehne, H.; Luebbers, T.; Meunier-Keller, N.; Mueller, F. Novel inhibitors of DNA gyrase: 3D structure based biased needle screening, hit validation by biophysical methods, and 3D guided optimization. A promising alternative to random screening. *J. Med. Chem.* **2000**, *43*, 2664–2674.
- (12) Leach, A. R.; Hann, M. M.; Burrows, J. N.; Griffen, E. J. Fragment screening: An introduction. *Mol. Biosyst.* **2006**, *9*, 430–446.
- (13) Xia, Z.; Knaak, C.; Ma, J.; Beharry, Z. M.; McInnes, C.; Wang, W.; Kraft, A. S.; Smith, C. D. Synthesis and evaluation of novel inhibitors of Pim-1 and Pim-2 protein kinases. *J. Med. Chem.* **2009**, *52*, 74–86.
- (14) Qian, K.; Wang, L.; Cywin, C. L.; Farmer, B. T. II; Hickey, E.; Homon, C.; Jakes, S.; Kashem, M. A.; Lee, G.; Leonard, S.; Li, J.; Magboo, R.; Mao, W.; Pack, E.; Peng, C.; Prokopowicz, A. III; Welzel, M.; Wolak, J.; Morwick, T. Hit to lead account of the discovery of a new class of inhibitors of Pim kinases and crystallographic studies revealing an unusual kinase binding mode. *J. Med. Chem.* **2009**, *52*, 1814–1827.
- (15) Congreve, M.; Carr, R.; Murray, C.; Jhoti, H. A rule of three for fragment-based lead discovery? *Drug Discovery Today* **2003**, *8*, 876–877.
- (16) *Glide (version 50207 unless otherwise mentioned)*; Schrödinger, Inc., New York, 2009; www.schrodinger.com
- (17) Berman, H. M.; Westbrook, J.; Feng, Z.; Gilliland, G.; Bhat, T. N.; Weissig, H.; Shindyalov, I. N.; Bourne, P. E. The Protein Data Bank. *Nucleic Acids Res.* **2000**, *28*, 235–242 (www.pdb.org).
- (18) Cheney, I. W.; Yana, S.; Appleby, T.; Walkera, H.; Voa, T.; Yao, N.; Hamatakea, R.; Honga, Z.; Wua, J. Z. Identification and structure–activity relationships of substituted pyridones as inhibitors of Pim-1 kinase. *Bioorg. Med. Chem. Lett.* **2007**, *17*, 1679–1683.
- (19) Pierce, A. C.; Jacobs, M.; Stuver-Moody, C. Docking study yields four novel inhibitors of the protooncogene Pim-1 kinase. *J. Med. Chem.* **2008**, *51*, 1972–1975.
- (20) Gampe, R. T. Jr.; Montana, V. G.; Lambert, M. H.; Miller, A. B.; Bledsoe, R. K.; Milburn, M. V.; Kliewer, S. A.; Willson, T. M.; Xu, H. E. Asymmetry in the PPARgamma/RXRalpha crystal structure reveals the molecular basis of heterodimerization among nuclear receptors. *Mol. Cell* **2000**, *5*, 545–555.
- (21) Pierce, A. C.; Sandretto, K. L.; Bemis, G. W. Kinase inhibitors and the case for CH...O hydrogen bonds in protein–ligand binding. *Proteins* **2002**, *49*, 567–576.
- (22) *Maestro (version 9.0 unless otherwise mentioned)*; Schrödinger, Inc., New York, 2009. www.schrodinger.com
- (23) *Vida version 3.1.* Open Eye Inc.; www.eyesopen.com
- (24) *Ligprep, version 22207*; Schrödinger, Inc., New York, 2009; www.schrodinger.com
- (25) Zhang, J. H.; Chung, T. D.; Oldenburg, K. R. A simple statistical parameter for use in evaluation and validation of high throughput screening assays. *J. Biomol. Screen* **1999**, 67–73.
- (26) Kumar, A.; Mandiyan, V.; Suzuki, Y.; Zhang, C.; Rice, J.; Tsai, J.; Artis, D. R.; Ibrahim, P.; Bremer, R. Crystal structures of protooncogene kinase Pim-1: A target of aberrant somatic hypermutations in diffuse large cell lymphoma. *J. Mol. Biol.* **2005**, *348*, 183–193.
- (27) Emsley, P.; Lohkamp, B.; Scott, W. G.; Cowtan, K. Features and development of Coot. *Acta Crystallogr.* **2010**, *66*, 486–501.